How efficient are thermoelectric materials? – an assessment of state-of-the-art individual and segmented thermoelectric materials

Lobato, C. Nuñez; Esposito, V.; Pryds, N.; Christensen, D.V.

Published in:
Materials Today Energy

Link to article, DOI:
10.1016/j.mtener.2024.101564

Publication date:
2024

Document Version
Peer reviewed version

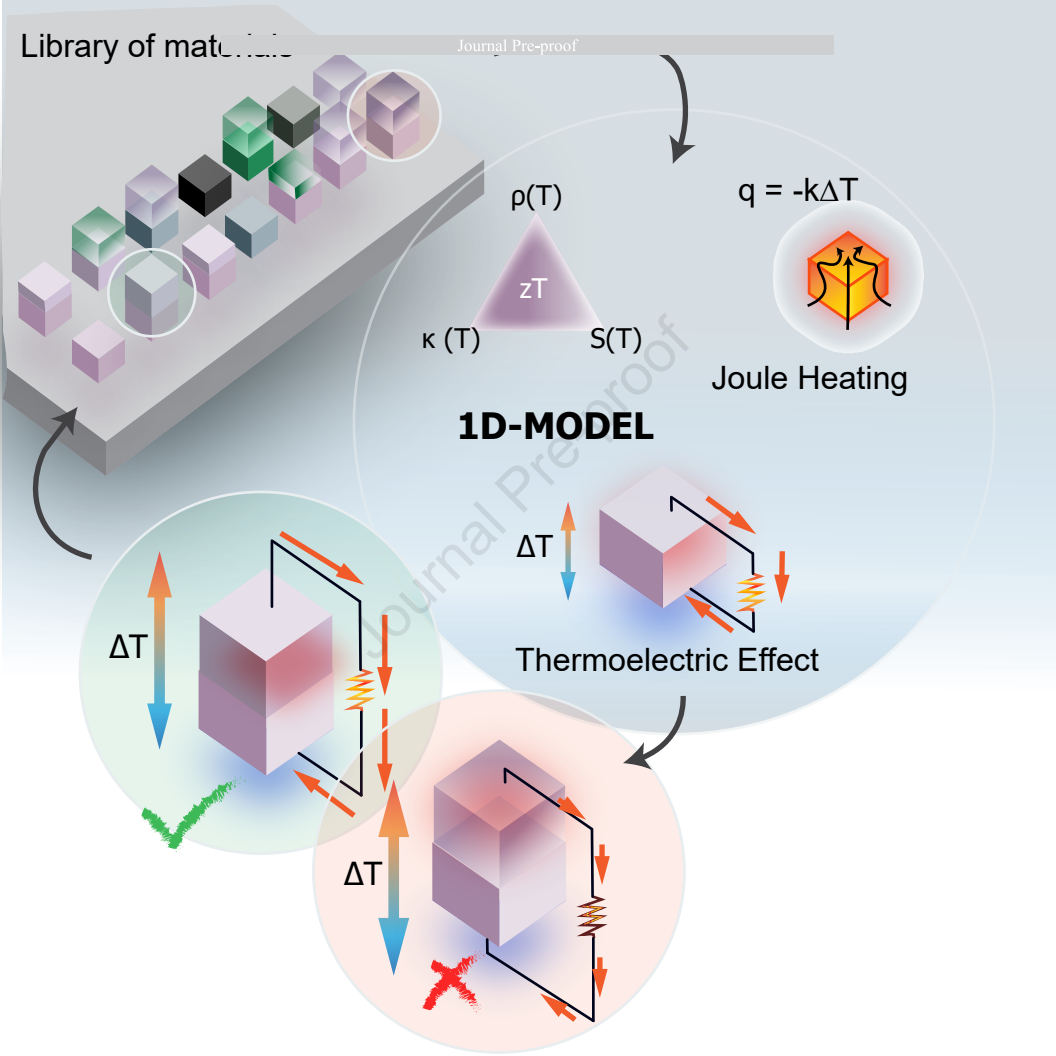

How efficient are thermoelectric materials?
– an assessment of state-of-the-art individual and segmented thermoelectric materials

C. Nuñez Lobato[1], V. Esposito[1], N. Pryds[1], D. V. Christensen[1]

[1]Department of Energy Conversion and Storage, Technical University of Denmark, DK-2800 Kgs. Lyngby, Denmark

Abstract

To efficiently convert heat into electricity using thermoelectric energy harvesting, it is essential to employ new material strategies. One effective approach is segmentation, where compatible materials optimized for different operating temperatures are combined to improve thermoelectric efficiency. Despite reports of severe efficiency reductions when segmenting incompatible materials, an updated assessment of the compatibility across state-of-the-art thermoelectric materials is missing. Here, we employ a numerical model to assess how efficiently non-segmented and segmented high-performing thermoelectric materials can convert heat into electricity. For the non-segmented materials, efficiency reaches up 17.9% at ΔT = 615 K without heat losses and contact resistances. Losses due to self-incompatibility were generally found to be small for most materials (< 0.6 percentage points) with few exceptions. In contrast, segmented thermoelectric legs were very sensitive to compatibility effects. Segmentation is found to only boost the efficiency significantly for $\Delta T > 300$ K. Here, we find efficiencies of up to 24% for p-type $AgSb_{0.94}Cd_{0.06}Te_2/Pb_{0.98}Te_{0.02}$-8%SrTe and 19% for n-type $Bi_{1.8S}Sb_{0.2}Te_{2.7}Se_{0.3}/Pb_{0.93}Sb_{0.05}S_{0.5}Se_{0.5}$. We further map out the maximum tolerable contact resistances before segmentation becomes detrimental. By providing an overview of the achievable energy conversion efficiencies, this study highlights the present state of thermoelectric energy conversion and critically assesses the prospects of segmentation.

Introduction

Thermal energy harvesting technologies have become increasingly important due to the vast amounts of waste heat stemming from industrial and domestic processes. One type of thermal energy harvester relies on thermoelectric (TE) materials to convert waste heat directly into electricity. Typically, the heat conversion efficiency of TE materials via the thermoelectric effect is evaluated using the dimensionless figure of merit $zT = \frac{\sigma S^2}{k}T$, where σ and k are the electrical and thermal conductivities, respectively, and S is the Seebeck coefficient. Thermoelectric research has long been devoted to improving the performance of TE materials by enhancing the figure of merit via (a) increasing the power factor (PF= σS^2) and (b) reducing the thermal conductivity. In the last decade, great advances in zT have been made with values far exceeding 2 in several material classes by employing strategies such as nanostructuring, alloying/doping and strain engineering [1–4]. Additionally, several significant challenges associated with TE materials have largely been improved, including scalability, brittleness and resource shortage [5,6].

Metallic tellurides (chalcogenides) are the best-performing TE materials at room and medium temperatures. These compounds comprise numerous compositions and structural variations, such as Bi_2Te_3 and $AgSbTe_2$-derivatives, which can display peak zT values between one and two at a temperature slightly below 400 K [7]–[8]. Due to the thermal instability of tellurides at high temperatures and their scarcity on Earth, there is an active effort towards finding alternative TE materials with a broader thermal window. For instance, zintl compounds particularly based on Mg_3Sb_2 have attracted recent attention as a possible candidate to compete with tellurides at room and medium temperatures (peak zT ~ 1-2) [9–14]. A collection of high-performing TE materials exhibiting exceptionally high zT approaching three, have been identified in the medium to high-temperature range (400-900 K), including compounds like SnSe [15,16], skutterudites [17], clathrates [17,18] or half-heuslers [19–21]. Other TE materials like $FeGa_3$-types [22,23], and oxides [24,25] also offer a competitive zT at high temperatures combined with elemental abundances.

In parallel to developing high zT materials, device fabrication has also been extensively investigated, emphasising the need to lower contact resistances [26–32] and exploring different device designs [33,34]. In a conventional thermoelectric generator (TEG), a pair of p- and n-type semiconductor legs are joined to form a unicouple, where each leg generates a voltage difference for a given thermal gradient via the Seebeck effect. Typically, the TE legs are connected electrically in series but thermally in parallel, such that numerous unicouples can be brought together to increase the voltage output. The optimal operating temperature of the constituent materials that make up either the n- or the p-type leg is determined by zT and the thermal stability of the leg, where the effects of a prolonged thermal gradient can irreversibly change the chemical structure of the TE-material over time. Hence, every TE leg displays an optimum zT-value within a specific temperature range, making the combination of materials in a single leg (segmentation) an attractive strategy to boost efficiency. This approach enables each leg of the unicouple in the TEG to function at its best when a larger temperature difference is applied, resulting in increased output power and efficiency compared to non-segmented legs exposed to the same temperature difference. For example, it has been shown experimentally that an optimized segmentation between Bi_2Te_3 and germanium telluride (GeTe) alloys can achieve an efficiency of 13.6% at ΔT = 493 K, which is among the highest measured values amongst segmented materials operating within the same temperature range [35]. Even good prospective modules with

segmented skutterudite-based thermoelectric legs can be found in the literature, as well as generators made up of newly discovered and high zT materials like GeTe and Mg_2Sb_3 [36].

However, finding the compatibility between TE materials, i.e., how well a set of thermoelectric materials can maintain optimal performance over a range of temperatures, is not trivial, as shown by Snyder and Ursell [37], and improper segmentation may even harm the efficiency. The compatibility factor was thus introduced in the early 2000's [37,38] to describe the optimal electric current necessary to achieve the highest efficiency. If the reduced current density matches the compatibility factor at any temperature along a TE leg, the maximum efficiency is obtained, which can be conveniently calculated from zT alone. However, in general, the reduced current density deviates from the compatibility factor, which reduces efficiency for both non-segmented and segmented legs. In particular, for segmented TE legs where each segment possesses a widely different compatibility factor, a significant mismatch between the reduced current density and compatibility factor is typically observed leading to a considerable reduction of efficiency [37]. For this reason, to efficiently match segments, the compatibility factors of each segment should not exceed a factor of two as a rule of thumb [37,38]. A few examples of improper segmentation were reported in Ref. [38], such as a TE leg consisting of p-TAGS materials ($(AgSbTe_2)_{0.15}(GeTe)_{0.85}$) and p-PbTe, yielding an efficiency even lower than that of p-TAGS alone at ΔT = 500 K. Additionally, Ngan *et al*. [39] performed an extensive investigation using a 1D model to numerically evaluate the performance of segmented TE legs and unicouples. For instance, at ΔT = 600 K, segmenting a leg with the three materials Bi_2Te_3, clathrate and $MnSi_2$, results in a reduction of almost 5 percentage points in efficiency compared to using only two segments since $MnSi_2$ acts as a non-matching compound [39]. Ngan *et al*. also assessed the most effective segmented thermoelectric legs at three distinct temperature gradients using state-of-the-art materials available in 2013. For instance, at a temperature difference of ΔT = 400 K, the p-type leg composed of materials in the family Bi_2Te_3/PbSrTe achieved an impressive efficiency of ~15 % ; at the same time, the n-type combination of Bi_2Te_3 and skutterudite delivered a notable ~13% efficiency.

Many effects may, however, negatively impact the final performance of the thermoelectric legs. While convective and radiative heat losses can be significantly reduced by proper insulation, contact resistances have hindered the further development of segmented thermoelectric legs. Here, the thermoelectric performance is lowered by (1) the contact resistances at the interfaces to the electrodes and (2) the interface between the two thermoelectric segments; both usually stemming from interfacial surface roughness or intermixing of elements. The interfaces between the thermoelectric segments have been addressed in a variety of TE legs [28,31,32,40–42] and have been reported to yield a similar order of magnitudes as the interfaces to the electrodes [27,39,43–48]: In the literature, reasonably low values for the specific electrical and thermal contact resistance have been reported (< 10^{-7} - 10^{-8} Ohm m^2 and 10^{-6}-10^{-8} m^2 W/K). Bjørk *et al.* (2015) [27] further numerically examined how the efficiency was affected by the electrical and thermal contact resistances between two thermoelectric segments for many segmented thermoelectric legs. Here, the authors identified a universal trend allowing an estimation of the maximum electrical and thermal contact resistance between material segments that can be tolerated before segmentation becomes worse than simply using the hot-side material alone.

Ouyang *et al*. [49] further evaluated segmented p- and n-type legs using 3D simulations by selectively choosing the best TE materials including the impact of contact resistances between the thermoelectric segments and the electrodes. Their results using geometrically asymmetric-sized unicouples, i.e. legs with a larger p-type area than n-type, showed that these modules could yield high efficiencies up to 20.9% when using p-$(Bi,Sb)_2Te_3$/MgAgSb/PbTeS/SnSe and n-CuBi2Te3Se/AgPbSbTe/SiGe segmented legs. As thermal and electrical contact resistances reached specific thresholds, the efficiency and

output power in the TEG module were shown to decline. However, TEG performance also exhibited a plateau below these threshold values, suggesting that if interfaces can be well controlled in each segmented leg, contact effects will not have a significant impact. Recently, Ryu *et al.* [1] further examined a more comprehensive library of materials using a high-throughput method, where they found segmented legs reaching a high efficiency of up to 24% at ΔT = 800 K. While the authors investigated TE efficiencies incorporating the temperature dependence of the thermoelectric properties, they did not consider compatibility matching between materials. Hence, despite numerous reports of segmentation, an updated compatibility assessment across state-of-the-art thermoelectric materials is needed.

To update the thermoelectric library of segmented materials and investigate new combinations with optimum conditions, we employ a 1D numerical model with a two-fold goal: (1) Evaluating the efficiency and degree of self-compatibility of non-segmented p- and n-type TE legs using a library of high zT materials. (2) Evaluating the efficiency and compatibility of segmented TE legs composed of two material segments with state-of-the-art zT values. This approach allows us to enhance thermoelectric materials and systems with updated high-performing materials.

Methods

We collected data on the thermoelectric properties of some of the highest zT materials for various temperatures in the best-performing TE material classes reported so far. The materials are grouped under well-recognized family categories with their chemical composition, material class and peak zT value displayed in Table 1. Although the area of thin-film thermoelectrics and low-dimensional systems has seen significant growth in recent decades [1,2,4,50,51], only bulk materials were reported in this paper.

We use a 1D model [37] to assess the efficiency and compatibility of non-segmented and segmented legs. This analysis is carried out as a function of an applied temperature gradient. The 1D model accounts for the most significant thermoelectric phenomena, namely the Peltier, Seebeck, and Thomson effects. It also considers the compatibility of the TE legs, heat conduction, Joule heating, and the temperature dependence of the intrinsic material properties, including the resistivity ($\rho = 1/\sigma$), Seebeck coefficient (S) and thermal conductivity (k). These properties and their temperature dependences can be found in Supplementary S1 for the selected material library. The temperature difference (ΔT) is defined as an input parameter by fixing a constant cold side temperature (T_c = 300 K) and varying the hot side (T_h) temperature of the leg, thereby creating a heat flow across the TE leg.

It should be noticed that thermal and electrical contact resistances and heat losses are excluded from the model. Their detrimental effects on the thermoelectric performance have been assessed elsewhere [1,27,49]. In real thermoelectric devices, thermoelectric legs are also three-dimensional, meaning heat flows in all directions instead of along the TE leg, as assumed in the 1D model. For a more complete understanding between heat transfer and a three dimensional geometry the reader is referred to Ref. [49,52]

The 1D model is expressed only in terms of the temperature and the intrinsic variables of the material, as already discussed in Ref. [37,53]. Instead of being a function of current and position, the 1D model introduces the so-called reduced current density $u = J/(k\Delta T)$, which is the ratio between the electrical current density (J) and the heat flux from heat conduction. Once the starting conditions of u are

defined at the hot side, $u_h=u(T=T_h)$, eq. (1) will determine the temperature profile of u throughout the TE leg [53]:

$$\frac{du(T)}{dT} = u^2 T \frac{dS(T)}{dT} + u^3 \rho(T) k \quad (1)$$

The solution to the reduced current density can be used to extract several properties, such as the thermoelectric efficiency, the heat flow along the leg, and the temperature profile, as described in more detail in [37,53]. The efficiency of the TE-leg can be calculated as eq. (2) [53],

$$\eta_{\text{leg}} = 1 - \frac{S_c T_c + \frac{1}{u_c}}{S_h T_h + \frac{1}{u_h}} , \quad (2)$$

where the subscripts refer to the hot (h) and cold (c) side of the TE leg. However, eq. (1) cannot be solved analytically due to the dependency of the material parameters on temperature, and we solve it recursively following eq. (3) [53],

$$\frac{1}{u_n} = \frac{1}{u_{n-1}} \sqrt{1 - 2u_{n-1}^2 \overline{\rho k}\,(T_n - T_{n-1})} - (T_n + T_{n-1})\bar{S} , \quad (3)$$

where the n-subscript denotes the step in temperature (T_n and T_{n-1}) and $\overline{\rho k}$ and $\bar{S}$ denote average of ρk and Seebeck between steps, respectively. Here, for a fixed hot side temperature, T_h , we select a starting condition $u_h = u_{n-1}$, that is employed to calculate the subsequent values of u_n, thereby recursively generating a profile of $u(T)$ that allows for finding a value for u_c. By varying the starting u_h condition, many $u(T)$ profiles over temperature can be generated according to eq. (3). We then evaluate the efficiency for each specific u_h using eq. (2) and select the $u(T)$ profile that yields maximum efficiency. This approach is equivalent to optimizing the power transfer between electronic circuits when performing impedance matching.

We further solve eq. (1) and (2) as a function of the hot side temperature (T_h) while keeping the cold side temperature constant at 300 K. Here, T_h was varied sequentially with a step size of 5 K over the full temperature range of the materials. Note that the profile of the optimum u(T) is determined by eq. (1) at every T_h. Thus, $u(\mathrm{T})$ may differ significantly from the ideal reduced current density (s) defined by the compatibility factor,

$$s(T) = \frac{\sqrt{1+zT}-1}{S(T)T}, \quad (4)$$

which is determined solely by intrinsic properties of the material [37]. Consequently, a drop in efficiency in the thermoelectric leg can be caused by the u-profile differing significantly from the compatibility factor either in a single material or when segmenting two dissimilar materials.

Eq. (1) is therefore used as well to model segmented legs, where the material properties along the legs are changed abruptly from one material to the other for a given interface temperature (T_i). In this report, the discussion is limited to segmented pairs, where we denote the hot (cold) segment as the material in the leg that operates at higher (lower) temperatures.

A rule of thumb to achieve beneficial leg segmentation between the cold and hot side materials lies in choosing compounds with compatibility factors differing by less than a factor of 2 [37,53]. In the ideal case where the profile of u-matches that of s, one obtains the theoretical maximum efficiency of the TE leg ($\eta_{(u=s)}$):

$$\eta_{(u=s)}=1 - \exp\left(-\int_{T_c}^{Th}\frac{\sqrt{1+zT}-1}{\sqrt{1+zT}+1}\frac{1}{T}\right). \qquad (5)$$

This expression is traditionally used to evaluate the efficiency of thermoelectric materials based only on temperature and zT. However, eq. (5) does not consider the mismatch between u(T) and *s(T)* that we here show can result in significant overestimations of the efficiencies in both non-segmented and segmented legs comprised of present state-of-the-art materials.

As the contact resistances and heat losses are excluded in the 1D model, the efficiency is independent of the length and cross-sectional area of the TE leg. However, following Bjørk *et al.* (2015), the maximum tolerable values for the specific electrical ($\rho_{c,el}^{max}$) or thermal contact resistance ($\rho_{c,th}^{max}$) can be extracted for segmented thermoelectric legs with two segments according to eq. (6) [27]:

$$\rho_{c,el/th}^{max} = \frac{g_{e/th}}{1-g_{e/th}} \cdot \rho_{leg} \cdot L, \qquad (6)$$

Here, ρ_{leg} denotes the average resistivity over the full segmented leg of length L, $g_{e/th}$ are universal contact resistance functions. Thus, one can find the maximum tolerable contact resistances through eq. (6), using the linear universal function expressions, $g_e = 0.72 \cdot \eta_{gain} + 7.09$ and $g_{th} = 0.56 \cdot \eta_{gain} + 2.32$, where $\eta_{gain}$is defined as the relative efficiency gain calculated in absence of contact resistances, i.e. $\eta_{gain} = (\eta_{segmented,leg} - \eta_{hot,leg})/\eta_{hot,leg}$. We note that the maximum tolerable contact resistances are independent of the cross-sectional area and linearly proportional to the length of the leg. The linear functions $g_{e/th}$ were found to describe a large number of segmented thermoelectric devices in a universal manner up to $\eta_{gain}\sim 50\%$, whereas segmented legs with larger gains were unaccounted for.

Results

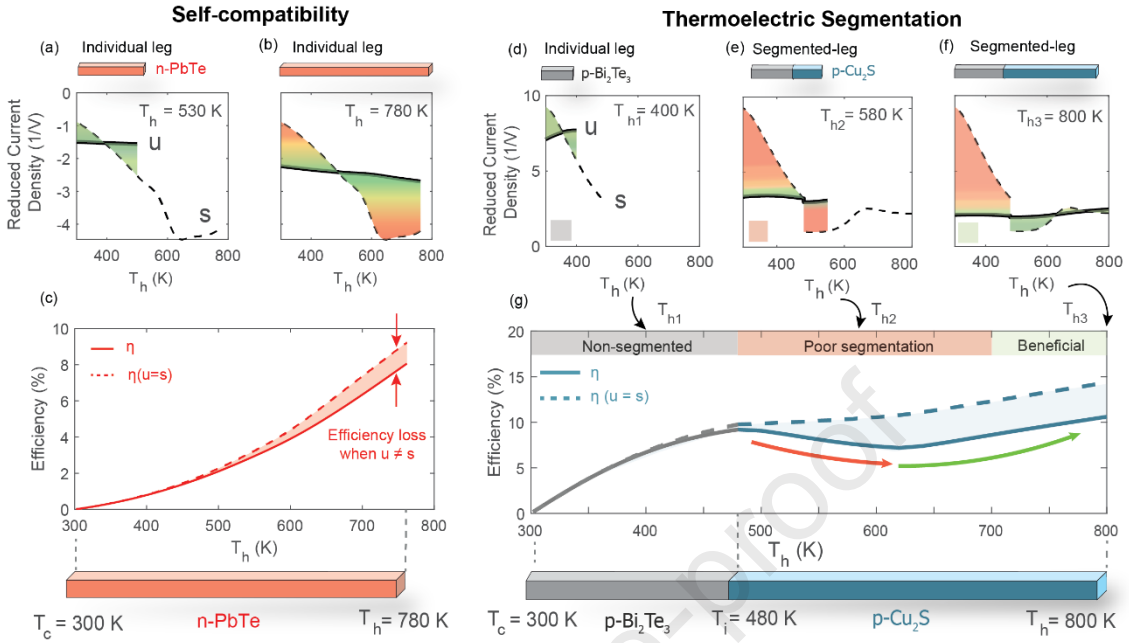

Fig. 1. A thermoelectric leg composed of one single material will experience different reduced current densities when T_h is varied from (a) a low T_h (b) to high T_h ; (c) The performance of the material in terms of efficiency (solid line) and theoretical maximum efficiency if u = s (dashed line) illustrates the idea of self-compatibility. For a segmented leg with two materials with non-matching compatibility factors, sweeping T_h determines the optimized profile of u in (d), (e) and (f), which can result in a negative or positive contribution to the efficiency of the overall leg, as shown in (g).

To illustrate the concept of the simulations, Figs. 1a-c show a non-segmented n-type leg within the parent family of n-PbTe, a material reported to have a large zT > 1.5 between 600 K to 800 K [54] (see Table 1 for more details). Fig. 1c displays the efficiency calculated using the 1D model as a function of the hot side temperature with a fixed cold side temperature of 300 K. The efficiency reaches a maximum of η ~ 7% (solid line) compared to $\eta_{(u=s)}$ ~ 8% (dashed line) corresponding to the reduced current density being equal to the compatibility factor at all temperatures, which is identical to calculating the efficiency directly from zT. Both efficiencies increase with the hot side temperature, but a significant discrepancy between η and $\eta_{(u=s)}$ also develops. Figs. 1a-b display the optimal reduced current density at hot side temperatures of 530 K and 780 K, together with the compatibility factor of the material. When the single leg is subjected to a moderate temperature gradient (T_h=530 K, ΔT=230 K), the material operates close to its maximum thermoelectric efficiency since the optimal current density u is close to the compatibility factor *s,* as observed in Fig. 1a. For larger gradients (T_h=780 K, ΔT=480 K), the difference between η and $\eta_{(u=s)}$ is caused by the large distance between *u* and *s* as shown in Fig. 1b. The nearly constant profile of u cannot accommodate the strongly temperature-dependent compatibility factor of n-PbTe, resulting in a 1.2 percentage points loss in efficiency (more information on the losses can be found in Supplementary S2). This loss thus originates from what we refer to as self-incompatibility effects.

For the case of a segmented leg, we illustrate the detrimental effect of segmentation on the efficiencies in Fig. 1g using two materials of the parent family p-Bi_2Te_3 and p-Cu_2S as the cold and hot sides of the leg, respectively. Here, p-Bi_2Te_3 has shown a zT of nearly 2 close to room temperature at 320 K [7], whereas p-Cu_2S reaches only a large zT > 1 at much higher temperatures close to 650 K [55] (see Table 1). Owing to the larger zT of p-Bi_2Te_3 at moderate temperatures compared to p-Cu_2S, we fix the

interface temperature T_i between p-Bi_2Te_3 and p-Cu_2S to 480 K, which corresponds to the highest temperature reported for the chosen compound in the category of p-Bi_2Te_3 [7]. The choice of the interface temperature between two segmented materials can significantly impact the resulting efficiency, as described in Supplementary Section S3. In this example of a segmented TE pair, a beneficial or negative effect from segmentation can be found depending on the applied temperature gradient the leg is subjected to. Starting with a non-segmented p-Bi_2Te_3 leg, Fig. 1d displays the behavior of u and s for a low-temperature gradient (T_h = 400K, ΔT=100 K) where only a small efficiency drop due to self-incompatibility can be observed (Fig. 1g). As the leg is segmented with p-Cu_2S and a relatively higher temperature gradient is applied (T_h = 580 K, ΔT=280 K), see Fig. 1e, the nearly constant profile of u deviates from the dissimilar compatibility factors of p-Bi_2Te_3 and p-Cu_2S. Here, s differs by up to an order of magnitude between the two materials, which impacts the overall efficiency negatively, as seen in Fig. 1g. Even a non-segmented p-Bi_2Te_3 leg exposed to a more moderate temperature gradient of ΔT = 180 K provides a higher efficiency compared to a segmented p-Bi_2Te_3 / Cu_2S leg as the temperature of hot side temperature reaches 740 K (ΔT = 440 K). However, when the temperature gradient is magnified (T_h = 800 K, ΔT=500 K), the overall match between u and s improves, as displayed in Fig. 1f, finally providing a beneficial segmentation. Even in this case, the final efficiency achieved (11%) at T_h = 800 K does not largely exceed that of the single material p-Bi_2Te_3 (9%) at 480 K. This significantly hampers the potential for segmenting these materials, especially when considering the added complexity in manufacturing, the extra electrical and thermal contact resistances that are introduced, and the accelerated degradation at elevated hot side temperatures.

Table 1. State-of-the-art thermoelectric materials displaying the material class, composition, peak zT value and at which temperature the peak zT value is obtained.

p-type				
Class	Composition	zT	T_{peak} (K)	Reference
Metalic Tellurides: Bi_2Te_3	$Bi_{0.5}Sb_{1.5}Te_3$	1.86	320	[7]
Metalic Tellurides: AgSbTe	$AgSb_{0.94}Cd_{0.06}Te_2$	2.6	573	[56]
Metalic Tellurides: PbTe-SrTe	$Pb_{0.98}Te_{0.02}$-8%SrTe	2.5	923	[57]
SnSe	$Na_{0.03}Sn_{0.965}Se$	3.1	783	[16]
Skutterudite	$Ce_{0.45}Nd_{0.45}Fe_3CoSb_{12}$	1.06	700	[58]
Zintl	$Ca_5In_{1.9}Zn_{0.1}Sb_6$	0.7	973	[59]
Clathrate	$Ba_8Ga_{15.8}Cu_{0.033}Sn_{30.1}$	0.9	450	[18]
FeGa3	$RuGa_{2.95}Zn_{0.05}$	0.75	620	[22]
Oxides	$Bi_{0.94}Pb_{0.06}Cu_{0.09}Fe_{0.01}SeO$	1.5	873	[25]
Half-Heusler-1 (HH-1)	$FeNb_{0.92}Hf_{0.08}Sb$	1.5	1200	[19]
Half-Heusler-2 (HH-2)	$(Nb_{0.6}Ta_{0.4})_{0.8}Ti_{0.2}FeSb$	1.6	1200	[20]
Sulfide: Cu_2S	$Cu_{1.97}S$	1.73	1000	[55]
Silicide	SiGe-4%TiO_2 nanoparticles	1.3	1100	[60]

n-type				
Class	Composition	zT	T_{peak} (K)	Reference
Metallic Tellurides: BiSbTeSe	$Bi_{1.85}Sb_{0.2}Te_{2.7}Se_{0.3}$	1.35	425	[8]
Metallic Tellurides: PbTe	PbTe-4%InSb	1.83	773	[54]
SnSe	SnSe	2.8	773	[15]
Skutterudite	$Ba_{0.08}La_{0.05}Yb_{0.04}Co_4Sb_{12}$	1.7	850	[61]
Half-Heusler (HH)	$(Hf_{0.3}Zr_{0.7})_{0.88}Nb_{0.12}CoSb$	1	1123	[21]
Zintl-1: Mg_3Sb_2	$Mg_{3.2}Bi_{1.5}Sb_{0.498}Te_{0.002}Cu_{0.01}$	1.1	357	[13]
Zintl-2: Mg_3Sb_2	$Mg_{3.16}$ $Bi_{0.69}Sb_{1.3}Te_{0.01}Mo_{0.04}$	1.84	680	[14]
Clathrate	$Ba_8Ga_{16.6}Ge_{28.7}$	1.14	773	[17]
$FeGa_3$	$Fe_{0.85}Co_{0.15}Ga_{2.65}Ge_{0.35}$	0.25	875	[23]
Oxide	$Sr_{0.95}(Ti_{0.8}Nb_{0.2})Ni_{0.05}O_{3-\delta}$ (reduced)	0.6	800	[24]
Selenide: PbS	$Pb_{0.93}Sb_{0.05}S_{0.5}Se_{0.5}$	1.7	900	[62]
Silicide	$Mg_2Si_{0.3}Sn_{0.7}$ + Bi and Cr	1.7	720	[63]
Sulfide: Bi_2SeS_2	$Bi_2Se_{0.88}Br_{0.12}S_2$	1.12	773	[64]
Sulfide: PbS	$Pb_{0.93}Sb_{0.05}S_{0.5}Se_{0.5}$	1.7	900	[65]

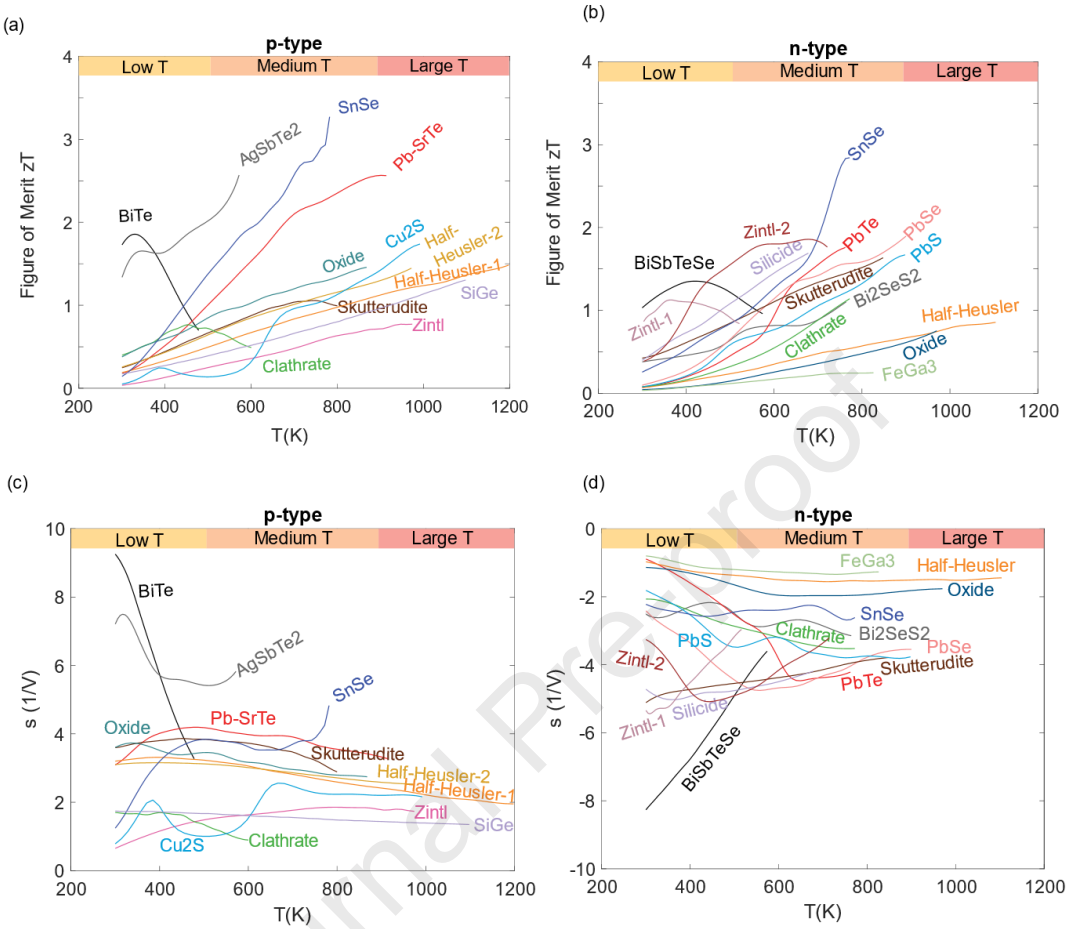

Fig. 2. Figure of merit (zT) for all individual thermoelectric (a) p-type and (b) n-type materials in Table 1. The compatibility factor of these materials is shown in (c) and (d) for p- and n-type materials, respectively.

To assess the reduction in efficiency due to self-compatibility effects and provide guidance to beneficial segmentation, we have collected the figures of merit (Figs. 2a-b) and calculated the corresponding compatibility factors (Figs. 2c-d) for a range of the state-of-the-art thermoelectric p- and n-type materials reported in the literature. Their specific compositions are described in Table 1, and their electrical conductivity, Seebeck coefficient, and thermal conductivity can be found in Fig. S1 in the Supplementary Material S1.

A key obstacle in constructing highly efficient and scalable TE modules lies in the scarcity of raw materials, such as tellurium; and their toxicity, like lead [2,5]. Alternative TE materials included in this study introduce elements like sulfur, silicon, oxygen, selenium, or magnesium, which benefit from higher abundance, lower prices and better safety profiles [2,5] despite having lower figures of merit in most cases (Figs. 2a-b). Another key concern is the thermal stability of TE legs subjected to large temperature gradients during operation. Common mechanisms of TE-degradation are sublimation of volatile dopants, diffusion within the TE-materials, and diminished contact performance. For instance, the volatility of certain elements and detrimental cation or vacancy diffusion at high temperatures is known for many materials, where efforts to reduce ion migration and modify the TE leg geometry have

been investigated [2,66,67]. One measure to protect against diffusion and sublimation of elements is e.g. to fill the space of TE-modules with inert gas but also cover their sides with materials that weaken sublimation and diffusion at high temperatures [67]. The stability, price and availability of these materials lies, however, beyond the scope of the present study, and the reader is referred to other publications for more in-depth studies hereof [2,5,6,66–68].

The materials in this study are not selected to broadly represent the respective material classes. Instead, they are examples selected due to their high figure of merit and well recognized published performance. In the low-temperature range (300-400K), p-type Bi_2Te_3 remains a champion material with a zT reaching 1.86 near room temperature [8],[15]. Similar alloys, namely $AgSbTe_2$ materials, show a competitive figure of merit, around 2.6, at the high end of this low-temperature region (T_h = 573 K) [56]. Competing with tellurides at room and medium temperatures, zintls materials like n-Mg_2Sb_3 with several doped elements have achieved high zT peak values of 1.1 at 357 K [13] and 1.8 at 650 K [14]. In this medium/high temperature span (600-800 K), SnSe was recently shown to have a zT above 3 at 783 K [16] as a p-type material and near 3 at 773 K in the n-type case [15]. On the other hand, a zT of around 1.8 and 1.25 at T = 773 K and 720 K was found in n-type PbTe [54] and zintl materials [69], respectively. For even higher temperatures (900-1200 K), p-PbTe-SrTe materials show a remarkable zT of 2.5 at T = 923 K [57], while recently reported n- and p-type half-Heusler's [19,20] dominate in the extremely high-temperature regime with a zT around 1 between 900 up to 1200 K.

Analogously to zT, the compatibility factor (s) is displayed in Figs. 2c-d, showing a strong temperature dependence, particularly for the p-type materials Bi_2Te_3, $AgSbTe_2$, and SnSe and n-type materials BiSbTeSe, Zintl-1, Zintl-2, PbTe, PbSe and Cu_2S. The overall compatibility factors can vary by more than an order of magnitude between materials, further motivating the present study on assessing efficient segmentation of high-performing TE materials. In Supplementary S3 (Fig. S3), we further provide the compatibility factor averaged across the full temperature range for all p- and n- materials as well as a simplified guide for selecting compatible materials.

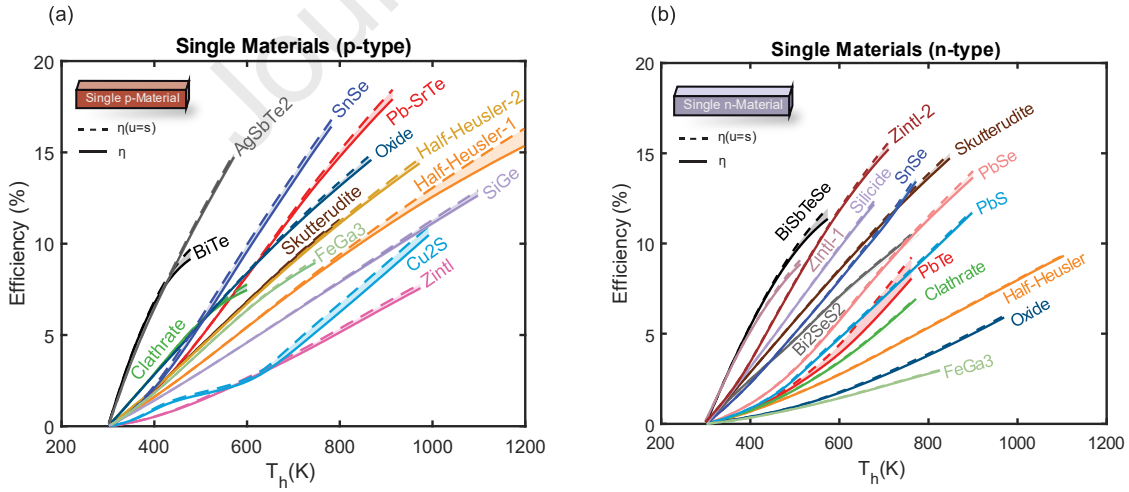

Fig. 3. Self-compatibility of individual (a) p-type and (b) n-type materials grouped by color. The solid line represents the efficiency as a function of the hot side temperature when taking self-compatibility into account. In contrast, the dashed line shows the theoretical maximum efficiency obtained when the reduced current density equals the compatibility factor at all temperatures.

The efficiency of a single thermoelectric leg calculated using the 1D model for the collected library of materials is shown as a function of the hot side temperature for p- and n-type in Figs. 3a-b. Among the p-type materials that exhibit the highest efficiencies, materials such as $AgSbTe_2$ (14.7%), SnSe (16.4%),

PbSrTe (17.9%) and half-Heuslers-2 (15.3%) reflect their high value of zT. Cu_2S is an interesting case with high zT = 1.74 at 992 K, which far exceeds the zT of the half-Heusler materials. However, the resulting efficiency of Cu_2S at 1000 K is significantly lower than for the half-Heuslers, owing to the drop in zT between 300 and 600 K. Among the n-type materials, BiSbTe (11.4%), Zintl-2 (15.0%), skutterudite (14.7%) and half-Heusler (9.32%) display the best efficiencies at low, medium and high temperatures. In addition, it is worth noting, the high performance at moderately low temperature gradients of the n-type material Zintl-1 which is highly competitive with n-type BiSbTe.

The dashed line in Figs. 3a-b displays the maximum efficiency for the ideal situation where $u = s$. The difference between these curves highlights the self-incompatibility of each individual material. Noticeably, there is a monotonic growing efficiency drop from the lack of self-compatibility with increasing temperature gradient. For most materials, the efficiency drop due to self-incompatibility is small (< 0.6 percentage points). However, a few materials, such as the high zT p-type half-Heusler-1 at T_h= 1200 K and n-type PbTe at T_h= 762 K, exhibit more notably efficiency losses of 0.95 and 1.17 percentage points, respectively. These results reflect that a strong temperature-dependent compatibility factor will often yield larger self-incompatibility losses. A more detailed view of the efficiency loss for each material is provided in Supplementary S2.

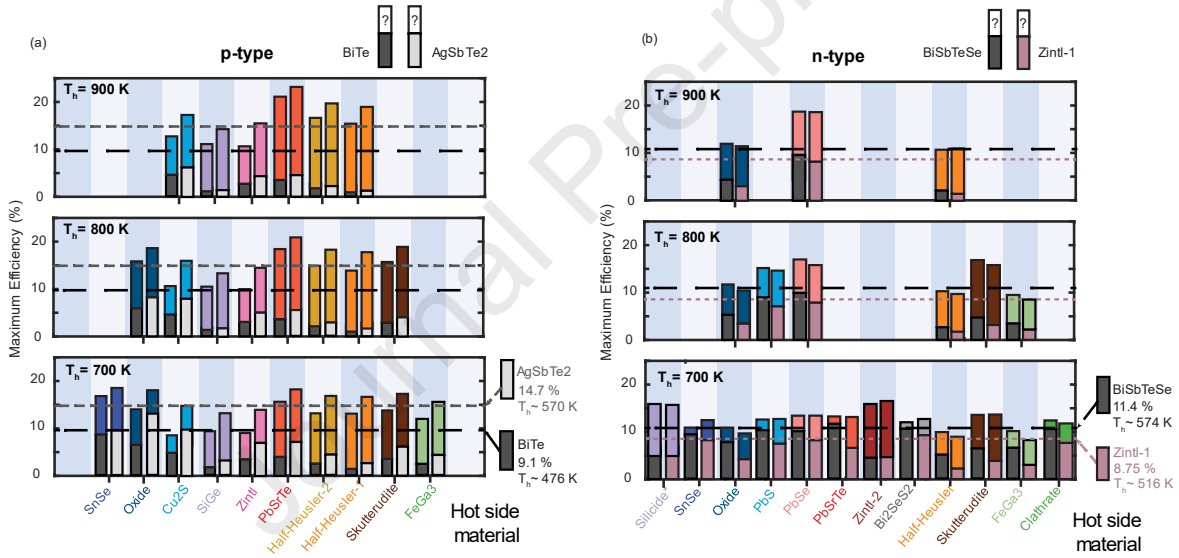

Fig. 4. Efficiency for segmented legs at three different hot side temperatures (T_h=700,800, and 900K) for (a) p-type, and (b) n-type materials. For the p-type legs, the cold-side material is fixed to either p-Bi_2Te_3 (dark gray) or $AgSbTe_2$ (light gray) and many hot side materials are evaluated. For the n-type legs, we fixed the cold-side segment to BiSbTeSe (dark gray) or silicide (purple). The interface temperature (Ti) is picked such as to optimize the maximum efficiency. Each segmented bar reflects the relative height of each material segment providing the highest efficiency. The efficiency of the cold side legs is also shown as horizontal dashed lines for reference.

We focus now on segmented legs comprising two segments where the boundary between the segments is characterized by an interface temperature (T_i). In the 1D model, the interface temperature can be directly translated into the spatial domain [53], which then describes to which extent the cold side and hot side segments take up the length of the leg. The interface temperature strongly impacts the resulting performance. Hence, we numerically optimize T_i and current density profile, u, to achieve the largest efficiency for all considered material pairs and hot side temperatures. In Supplementary S4, we compare this with two simpler approaches to finding T_i, namely (1) T_i is selected to be the temperature that maximizes zT everywhere in the leg [39] and (2) T_i is selected as the temperature where the s-profiles of the two segmented materials intersect [37,53]. The first approach yields interface temperatures and efficiencies close to the optimum values for nearly all materials. In

contrast, the second approach yields significant deviations in interface temperature and resulting efficiency.

For the cold segment, we chose either Bi_2Te_3 or $AgSbTe_2$ in p-type thermoelectric legs and BiSbTeSe or Zintl-1 in the n-type legs. These materials were selected due to their high efficiency near room temperature. For the non-segmented p-type legs, Bi_2Te_3 and $AgSbTe_2$ reach 9.1% and 14.7% in efficiency at their highest reported T_h ~ 476 K and ~ 570 K, respectively (see Fig. 3a). Conversely, n-type non-segmented legs made up of BiSbTeSe and Zintl-1 reach efficiencies of 11.4% and 8.75% at T_h ~ 574 and 516 K, respectively (see Fig. 3b). However, these high-performing materials at low temperatures possess strongly temperature-dependent compatibility factors (see Fig. 2c-d), which may hamper beneficial segmentation. The compatibility factors of p-Bi_2Te_3, p-$AgSbTe_2$ as well as n-BiSbTeSe and n-Zintl-1 change by a factor of 2.9, 1.3, 3 and 1.8 across their reported temperature range, respectively. Nonetheless, when evaluating the average compatibility factor of these cold segments across their entire temperature range, they still show the potential to be efficiently segmented with most materials (see Supplementary S3).

Fig. 4 displays the resulting efficiency when combining the selected cold-side segments with the material library. The results are shown for three hot-side temperatures T_h = 700 K, 800 K and 900 K (bottom, middle and top panel) while fixing the cold side at T_c = 300 K. For all hot-side temperatures and material combinations, we numerically optimize the interface temperature and the reduced current density profile. We translate the interface temperature to the spatial domain and display the relative lengths of the hot and cold side materials with the colored bars in Figure 4. (see Supplementary S5 for further information on the relative lengths of the segments)

Overall, the relative length of the hot segment material increases with the hot side temperature. For instance, when p-type SnSe is segmented with p-type Bi2Te3 at T_h = 700 K shown in the bottom panel of Fig. 4a, both the grey and blue bars have equal heights, implying that the optimal leg has roughly 50% p-SnSe and 50% of p-Bi2Te3. As T_h is raised to 900 K, the relative length of p-SnSe in the leg becomes 61% of the total leg. In contrast, for n-type legs with segmented n-type BiSbTeSe/SnSe at T_h = 700 K (bottom panel of Fig. 4b), the optimal solution is composed mostly (65%) of the n-type BiSbTeSe segment. Note that if the solution only contained the hot-side material without segmentation, the optimum interface temperature would be reduced to 300 K, and only a single material color would be present. This is not the case for any material combinations except for p-Bi2Te3/Clathrate as shown in Supplementary S4, signifying the gain in efficiency with respect to the hot side material alone by adding a high-performing cold side material to the hot segment.

The largest segmentation gains were found when comparing the efficiencies of the segmented legs with those of the individual hot side materials (see Supplementary S6 for an overview hereof). Here, non-segmented p-type Cu_2S and n-type $FeGa_3$ displaying efficiencies of 4.1% and 2.1% at T_h = 700 K (Fig. 3a-b), can be enhanced by 10.7 and 7.6 percentage points when segmented as p-$AgSbTe2/Cu_2S$ leg and a n-Zintl-1/FeGa3 leg, respectively. The segmentation gain with respect to the efficiency of the individual hot segment can, however, be marginal in other cases, such as for n-BiSbTeSe/SnSe (0.90 percentage points) and n-Zintl-1/Zintl-2 (1.33 percentage points) at T_h = 700 K.

In contrast, efficiency benefits from segmentation can be challenged if we now compare the segmentation gain at T_h = 700-900 K with the efficiencies of non-segmented cold-side materials between 476 and 678 K (i.e. maximum reported temperature for the cold side legs). For instance, non-segmented legs of n-type BiSbTeSe can achieve an efficiency of 11.4% at its highest T_h ~ 574 K (dashed line in Figure 4b); however, a segmented n-type leg of n-BiSbTeSe/HH yields 9.76% at T_h=700 K (Fig. 4b), making the non-segmented leg with a lower temperature gradient a better choice. Note that

segmented n-type BiSbTeSe/HH still provides gains in efficiency compared to its hot side counterpart operating independently (n-HH yields 4% efficiency at T_h=700 K i.e. a gain of 5 pp when segmented). Thus, using a single material leg with BiSbTeSe and a reduced the thermal gradient would be the preferred choice in this case. Otherwise, adding, e.g., a passive material to the non-segmented leg can also be an alternative solution to keep the cold segment operating in its thermal stability window. Interestingly, this trend is frequently observed at Th = 700 K, where many segmented legs do not exhibit a strongly increased efficiency compared to that achieved by the non-segmented cold-side material (see Fig. S5).

In general, efficiencies for the p-types are larger than for n-type materials due to their higher average zT in this p-type material selection. When highlighting the case of T_h= 900 K (ΔT=600 K), the p-type segmented legs that reach the highest efficiencies are the following combinations: p-$AgSbTe_2$/PbSrTe (23%), p-Bi2Te3/PbSrTe (21.5%) and p-AgSbTe2/HH-1 (19.6%). This value exceeds the maximum efficiency of less than 20% at T_h= 900 K, calculated using the same methodology in Ref. [39] and of the best segmented legs found in Ref. [1,49] with state-of-the-art materials. The best-performing n-type segmented legs were n-Bi2Te3/PbSe (18.9%) and n-Zintl-1/PbSe (18.4%) at T_h= 900 K, also with values exceeding those found in Ref.[1,39,49].

Segmentation introduces, however, an additional interface in the TE leg with associated electrical and thermal contact resistances, which is highly material specific. To provide guidance on the maximum electrical ($\rho_{c,el}^{max}$) and thermal ($\rho_{c,th}^{max}$) contact resistances that segmented thermoelectric legs can tolerate before segmentation becomes detrimental – compared the non-segmented hot-side material – we have plotted Fig. 5a-b for p- and n- type materials at T_h= 700 K (ΔT = 400 K) following the work by Bjørk *et al.* [27] (see eq. (6)). We note that the maximum tolerable values increase linearly with the length of the leg and we hence fix the length of the leg to L = 1 cm. In addition, as Bjørk's model was only validated for a limited range of segmented efficiency gains.Hence, the maximum tolerable contact resistances are only shown for material pairs within this validated range. For more information on the relative efficiency gains, see Supplementary S6.

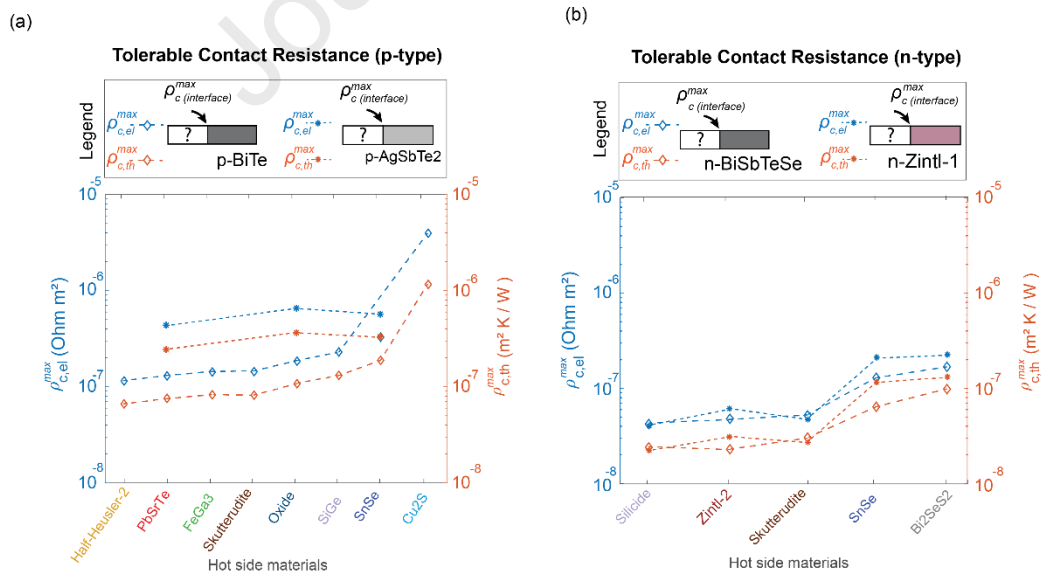

Fig. 5. Maximum tolerable specific electrical ($\rho_{c,el}^{max}$) and thermal ($\rho_{c,th}^{max}$)contact resistances at T_h = 700 K in electrical (blue) and thermal (orange) resistivity for segmented (a) p-type legs using either p-Bi2Te3 (diamonds) or p-AgSbTe2 (stars) as the cold side and (b) n-type legs using n-BiSbTeSe (diamonds) or n-Zintl-1 (stars) as the cold side. The total length of the segmented leg in this calculations was L = 1 cm.

Above these maximum tolerable contact resistances, the selected segmented pairs will not benefit from any gain in efficiency at T_h = 700 K compared to just using the hot-side materials alone at the same temperature. For example, in Fig. 5a, p-PbSrTe acting as a single leg shows an efficiency of 11.8 % at T_h = 700 K; however, when segmented as a pair p-Bi_2Te_3/PbSrTe, the gain in efficiency with respect to the hot side is 3.9 percentage points. Hence, this segmented leg shows an increase of $\Delta\eta_{gain}$~ 33 % with respect to the hot side, which translates into maximum tolerable contact resistances of $\rho^{max}_{c,el}$= 1.3x10^{-7} Ω m^2 and $\rho^{max}_{c,th}$= 7.6x10^{-8} m^{2}W/K. When using an alternative cold side, the segmented leg p-AgSbTe2/PbSrTe achieves a higher efficiency of 18.4 % at T_h = 700 K, i.e. a gain of 6.59 percentage points with respect to the hot side alone ($\Delta\eta_{gain}$~ 56 %). Therefore, it will possess a larger tolerable contact resistance, namely, $\rho^{max}_{c,el}$= 4.4 ·10^{-7} Ω m^2 and $\rho^{max}_{c,th}$= 2.5 · 10^{-7} m^{2}W/K. In practice, the maximum tolerable electrical contact resistances found in Figs. 5a-b are on the same order of magnitude as the typical low experimental values found in the literature with $\rho_{c,el}$ ~ 10^{-8} to 10^{-6} Ω m^2 [27,39,43–48]. However, the estimation of the tolerable thermal contact resistance is conservative in most cases, which is typically reported be in the range of $\rho_{c,th}$ ~ 10^{-6} - 10^{-3} m^{2}W/K [41,43–45].

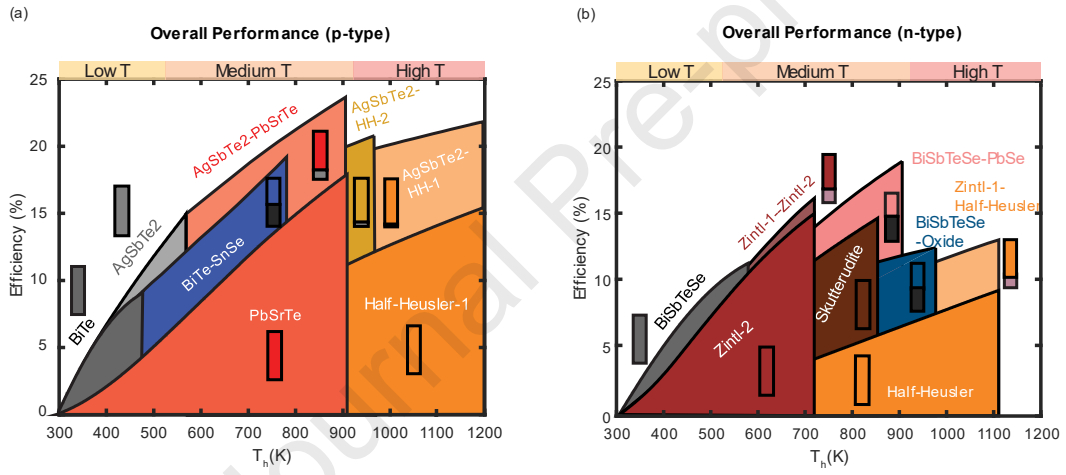

Fig. 6. Efficiency of single and segmented legs at different hot side temperatures displayed for (a) n-type materials and (b) p-type materials.

Figs. 6a-b display a map of efficiencies as a function of hot side temperature for the best-performing non-segmented and segmented legs. The segmented and individual material legs with lower efficiencies than those in Figs. 6a-b are not shown here for clarity in favor of the best performing legs. Attached to each curve are bars representing the optimized relative lengths of the cold and hot side materials. Once again, p-type materials in Fig. 5a show overall higher efficiency compared to the n-type materials in Fig. 5b. For reference, the highest efficiency curves are lower than the Carnot efficiencies, η_{Carnot} = 1-T_c/T_h, by a factor of roughly 0.35 for the p-types and 0.29 for the n-type materials.

Among the p-type legs at low hot side temperatures, $AgSbTe_2$ is a high-performing non-segmented leg, reaching a maximum efficiency of 14.7% at T_h= 570 K. Up until that temperature, the maximum efficiency of this non-segmented leg is larger than what could be achieved with any segmented leg. As a non-segmented leg also benefits from fewer interfaces, segmentation would only be detrimental in this low-temperature region (ΔT < 300 K) due to the addition of adverse thermal and electrical contact resistances. At higher temperatures (ΔT > 300 K), several segmented legs provide outstanding

optimized efficiencies, such as p-AgSbTe2/PbSrTe (24% at T_h = 915 K) and p-AgSbTe2/HH-2 (20.7% at T_h = 972 K), keeping maximum specific contact resistances according to Fig. 5a below $\rho_{c,el}$= 4.4 ·10^{-7} Ω m^2 and $\rho_{th,el}$= 2.5 · 10^{-7} m^2W/K and $\rho_{c,el}$= 6.7 ·10^{-7} Ω m^2 and $\rho_{c,th}$= 3.0 · 10^{-7} m^2W/K, respectively. These high efficiencies are partly due to (1) the large thermal gradient that the leg is subjected to, (2) their individually high zT and (3) a decent overall compatibility of the combined materials. A striking feature is that increasing the hot side temperature beyond 915 K does not show any significant increase in efficiency. This is in close agreement with the findings from Ryu *et al.* [1], owing to the lack of compatible high-zT materials at these temperatures and low average zT values.

Among the n-type legs, non-segmented BiSbTeSe achieves the highest efficiency, up to 11.4% at T_h = 574 K. We also highlight the high performance up to T_h = 715 K of Zintl-2 as a single leg with an efficiency of 15.1 % exceeding that of many segmented pairs even at higher temperature gradients. The segmented pair n-Zintl-1/Zintl-2 simultaneously achieves 16.4 %, however, with maximum tolerable contact resistances of $\rho_{c,el}$= 6.0 ·10^{-8} Ω m^2 and $\rho_{c,th}$= 3.1 · 10^{-8} m^2W/K according to Fig. 5b. The monotonic efficiency increase with temperature continues when segmenting BiSbTeSe with PbSe, reaching a 18.9% at 900 K. Note that this segmented pair at a lower at T_h= 700 K displayed a maximum tolerable contact resistance of $\rho_{c,el}$= 1.7 ·10^{-8} Ω m^2 and $\rho_{c,th}$= 9.8 · 10^{-8} m^2W/K. In the medium temperature region (300 K < ΔT < 550 K), the non-segmented n-skutterudite material presented a good alternative to segmented legs, reaching an efficiency 14.5% at T_h = 820 K. For a higher gradient, the pair n-BiSbTe/Oxide displayed 12.4% at T_h = 970 K and n-Zintl-1/Half-Heusler with 13.1% at T_h = 1104 K. As observed, only segmentation of n-BiSbTeSe/PbSe gave a noticeable boost in efficiency out of all the n-type material combinations considered.

When considering the chosen material library, we can deduce that if T_h < 600 K (ΔT < 300 K), segmentation of thermoelectric materials does not provide significant efficiency gains over non-segmented legs. Hence, single material legs with high figures of merit, such as p-type Bi_2Te_3 and $AgSbTe_2$ or n-type BiSbTeSe and n-Zintl-1, can be used instead. On the other hand, more noticeable efficiency gains are found for larger thermal gradients ΔT > 300 K, with segmented combinations that display good compatibility, such as p-$AgSbTe_2$/PbSrTe and n-BiSbTeSe/PbSe. While the results of these simulations can only be considered as an upper boundary for efficiency, maintaining these high-temperature gradients on the TE legs will bring about other issues, such as diffusion or intermixing at the interface, together with chemical instability of the materials; effects not considered in this study. In addition, we stress again other important factors to making scalable TE legs, such as (1) available and abundant materials, (2) large thermal and cycling stability, and (3) reduced thermal and electrical contact resistances of these materials.

Conclusion

The efficiency of state-of-the-art thermoelectric materials was calculated using the 1D model, considering their compatibility factors. Non-segmented materials displaying large changes in the compatibility factor will exhibit the largest loss in efficiency due to self-compatibility effects. At medium-temperature gradients, noticeable efficiency losses can be seen in p-Bi2Te3 (0.53 percentage points) and n-BiSbTeSe (0.60 percentage points), but in general it is overall low. In comparison, at high-temperature gradients, we find materials with a more noticeable efficiency loss, such as p-PbSrTe (0.52 percentage points), p-half-Heusler-1 (0.95 percentage points) or n-PbTe (1.17 percentage points). Among the single legs that exhibit the highest efficiencies ΔT > 300 K, p-SnSe (16.4%), p-PbSrTe (17.9%) are very competitive at high temperatures, together with n-Zintl-2 (15.0%) and n-skutterudite (14.7%).

When pairing materials into a TE leg, a careful choice must be made by looking at their compatibility factors. The efficiency gain of segmentation is marginal at $\Delta T < 300$ K when compared to the efficiency of high-performing non-segmented legs. Above $\Delta T > 300$ K, e.g. at $T_h = 900$ K, segmented pairs like p-$AgSbTe_2$/PbSrTe (23%), p-Bi_2Te_3/PbSrTe (21.5%), p-$AgSbTe_2$/PbSrTe (19.6%) or n-Bi_2Te_3/PbSe (18.9%) are examples of beneficial segmentation boosting the efficiency compared to the individual materials. The maximum efficiency achieved by segmentation was p-$AgSbTe_2$/PbSrTe (24.0%) at $T_h = 915$ K and n-Bi_2Te_3/PbSe (18.9%) at $T_h = 900$ K. While the results of these simulations can only be considered as an upper boundary for efficiency, they also highlight a path for significant improvements in the current TE performance and the need for a careful selection of materials when segmentation is done in a TE-pair.

References

[1] B. Ryu, J. Chung, M. Kumagai, T. Mato, Y. Ando, S. Gunji, A. Tanaka, D. Yana, M. Fujimoto, Y. Imai, Y. Katsura, S. Park, Best thermoelectric efficiency of ever-explored materials, iScience 26 (2023) 106494. https://doi.org/10.1016/j.isci.2023.106494.

[2] R. Freer, D. Ekren, T. Ghosh, K. Biswas, P. Qiu, S. Wan, L. Chen, S. Han, C. Fu, T. Zhu, A.K.M. Ashiquzzaman Shawon, A. Zevalkink, K. Imasato, G.J. Snyder, M. Ozen, K. Saglik, U. Aydemir, R. Cardoso-Gil, E. Svanidze, R. Funahashi, A.V. Powell, S. Mukherjee, S. Tippireddy, P. Vaqueiro, F. Gascoin, T. Kyratsi, P. Sauerschnig, T. Mori, Key properties of inorganic thermoelectric materials—tables (version 1), J. Phys. Energy 4 (2022) 022002. https://doi.org/10.1088/2515-7655/ac49dc.

[3] G.J. Snyder, E.S. Toberer, Complex thermoelectric materials, Nature Mater 7 (2008) 105–114. https://doi.org/10.1038/nmat2090.

[4] Y. Sun, Y. Liu, R. Li, Y. Li, S. Bai, Strategies to Improve the Thermoelectric Figure of Merit in Thermoelectric Functional Materials, Frontiers in Chemistry 10 (2022). https://www.frontiersin.org/articles/10.3389/fchem.2022.865281 (accessed October 16, 2023).

[5] J. Zhang, L.R. Jørgensen, L. Song, B.B. Iversen, Insight into the Strategies for Improving the Thermal Stability of Efficient N-Type Mg3Sb2-Based Thermoelectric Materials, ACS Appl. Mater. Interfaces 14 (2022) 31024–31034. https://doi.org/10.1021/acsami.2c07457.

[6] L.R. Jørgensen, B.B. Iversen, Characterizing thermoelectric stability, Dalton Trans. 51 (2022) 3807–3816. https://doi.org/10.1039/D1DT04001D.

[7] S.I. Kim, K.H. Lee, H.A. Mun, H.S. Kim, S.W. Hwang, J.W. Roh, D.J. Yang, W.H. Shin, X.S. Li, Y.H. Lee, G.J. Snyder, S.W. Kim, Dense dislocation arrays embedded in grain boundaries for high-performance bulk thermoelectrics, Science 348 (2015) 109–114. https://doi.org/10.1126/science.aaa4166.

[8] B. Zhu, X. Liu, Q. Wang, Y. Qiu, Z. Shu, Z. Guo, Y. Tong, J. Cui, M. Gu, J. He, Realizing record high performance in n-type Bi2Te3-based thermoelectric materials, Energy Environ. Sci. 13 (2020) 2106–2114. https://doi.org/10.1039/D0EE01349H.

[9] K. Imasato, S.D. Kang, G.J. Snyder, Exceptional thermoelectric performance in Mg3Sb0.6Bi1.4 for low-grade waste heat recovery, Energy Environ. Sci. 12 (2019) 965–971. https://doi.org/10.1039/C8EE03374A.

[10] Z. Liu, N. Sato, W. Gao, K. Yubuta, N. Kawamoto, M. Mitome, K. Kurashima, Y. Owada, K. Nagase, C.-H. Lee, J. Yi, K. Tsuchiya, T. Mori, Demonstration of ultrahigh thermoelectric efficiency of ~7.3% in Mg3Sb2/MgAgSb module for low-temperature energy harvesting, Joule 5 (2021) 1196–1208. https://doi.org/10.1016/j.joule.2021.03.017.

[11] X. Chen, J. Zhu, D. Qin, N. Qu, W. Xue, Y. Wang, Q. Zhang, W. Cai, F. Guo, J. Sui, Excellent thermoelectric performance of boron-doped n-type Mg3Sb2-based materials via the

manipulation of grain boundary scattering and control of Mg content, Sci. China Mater. 64 (2021) 1761–1769. https://doi.org/10.1007/s40843-020-1559-4.
[12] J. Lei, H. Wuliji, K. Zhao, T.-R. Wei, Q. Xu, P. Li, P. Qiu, X. Shi, Efficient lanthanide Gd doping promoting the thermoelectric performance of Mg3Sb2-based materials, J. Mater. Chem. A 9 (2021) 25944–25953. https://doi.org/10.1039/D1TA07988C.
[13] Z. Liu, W. Gao, H. Oshima, K. Nagase, C.-H. Lee, T. Mori, Maximizing the performance of n-type Mg3Bi2 based materials for room-temperature power generation and thermoelectric cooling, Nat Commun 13 (2022) 1120. https://doi.org/10.1038/s41467-022-28798-4.
[14] L. Wang, N. Sato, Y. Peng, R. Chetty, N. Kawamoto, D.H. Nguyen, T. Mori, Realizing High Thermoelectric Performance in N-Type Mg3(Sb, Bi)2-Based Materials via Synergetic Mo Addition and Sb–Bi Ratio Refining, Advanced Energy Materials 13 (2023) 2301667. https://doi.org/10.1002/aenm.202301667.
[15] C. Chang, M. Wu, D. He, Y. Pei, C.-F. Wu, X. Wu, H. Yu, F. Zhu, K. Wang, Y. Chen, L. Huang, J.-F. Li, J. He, L.-D. Zhao, 3D charge and 2D phonon transports leading to high out-of-plane ZT in n-type SnSe crystals, Science 360 (2018) 778–783. https://doi.org/10.1126/science.aaq1479.
[16] C. Zhou, Y.K. Lee, Y. Yu, S. Byun, Z.-Z. Luo, H. Lee, B. Ge, Y.-L. Lee, X. Chen, J.Y. Lee, O. Cojocaru-Mirédin, H. Chang, J. Im, S.-P. Cho, M. Wuttig, V.P. Dravid, M.G. Kanatzidis, I. Chung, Polycrystalline SnSe with a thermoelectric figure of merit greater than the single crystal, Nat. Mater. 20 (2021) 1378–1384. https://doi.org/10.1038/s41563-021-01064-6.
[17] B. Sun, X. Jia, D. Huo, H. Sun, Y. Zhang, B. Liu, H. Liu, L. Kong, B. Liu, H. Ma, Effect of High-Temperature and High-Pressure Processing on the Structure and Thermoelectric Properties of Clathrate Ba8Ga16Ge30, J. Phys. Chem. C 120 (2016) 10104–10110. https://doi.org/10.1021/acs.jpcc.6b02678.
[18] Y. Saiga, B. Du, S.K. Deng, K. Kajisa, T. Takabatake, Thermoelectric properties of type-VIII clathrate Ba8Ga16Sn30 doped with Cu, Journal of Alloys and Compounds 537 (2012) 303–307. https://doi.org/10.1016/j.jallcom.2012.05.049.
[19] C. Fu, S. Bai, Y. Liu, Y. Tang, L. Chen, X. Zhao, T. Zhu, Realizing high figure of merit in heavy-band p-type half-Heusler thermoelectric materials, Nat Commun 6 (2015) 8144. https://doi.org/10.1038/ncomms9144.
[20] J. Yu, C. Fu, Y. Liu, K. Xia, U. Aydemir, T.C. Chasapis, G.J. Snyder, X. Zhao, T. Zhu, Unique Role of Refractory Ta Alloying in Enhancing the Figure of Merit of NbFeSb Thermoelectric Materials, Advanced Energy Materials 8 (2018) 1701313. https://doi.org/10.1002/aenm.201701313.
[21] Q. Qiu, Y. Liu, K. Xia, T. Fang, J. Yu, X. Zhao, T. Zhu, Grain Boundary Scattering of Charge Transport in n-Type (Hf,Zr)CoSb Half-Heusler Thermoelectric Materials, Advanced Energy Materials 9 (2019) 1803447. https://doi.org/10.1002/aenm.201803447.
[22] D. Kasinathan, M. Wagner, K. Koepernik, R. Cardoso-Gil, Yu. Grin, H. Rosner, Electronic and thermoelectric properties of RuIn 3 − x A x (A = Sn, Zn), Phys. Rev. B 85 (2012) 035207. https://doi.org/10.1103/PhysRevB.85.035207.
[23] V. Ponnambalam, D.T. Morelli, Improved thermoelectric properties in heavily doped FeGa3, Journal of Applied Physics 118 (2015). https://doi.org/10.1063/1.4938474.
[24] S. Hirata, M. Ohtaki, K. Watanabe, Highly improved thermoelectric performance of Nb-doped SrTiO3 due to significant suppression of phonon thermal conduction by synergetic effects of pores and metallic nanoparticles, Ceramics International 46 (2020) 25964–25969. https://doi.org/10.1016/j.ceramint.2020.07.085.
[25] L. Pan, Y. Lang, L. Zhao, D. Berardan, E. Amzallag, C. Xu, Y. Gu, C. Chen, L.-D. Zhao, X. Shen, Y. Lyu, C. Lu, Y. Wang, Realization of n-type and enhanced thermoelectric performance of p-type BiCuSeO by controlled iron incorporation, J. Mater. Chem. A 6 (2018) 13340–13349. https://doi.org/10.1039/C8TA03521K.
[26] L. Ga, S. Huang, Y. Zhang, D. Xu, W. Li, Thermal resistances model for a soil-to-air thermoelectric generator device, Case Studies in Thermal Engineering 39 (2022) 102475. https://doi.org/10.1016/j.csite.2022.102475.

[27] R. Bjørk, The Universal Influence of Contact Resistance on the Efficiency of a Thermoelectric Generator, Journal of Elec Materi 44 (2015) 2869–2876. https://doi.org/10.1007/s11664-015-3731-7.
[28] J. Camut, S. Ayachi, G. Castillo-Hernández, S. Park, B. Ryu, S. Park, A. Frank, C. Stiewe, E. Müller, J. de Boor, Overcoming Asymmetric Contact Resistances in Al-Contacted Mg2(Si,Sn) Thermoelectric Legs, Materials (Basel) 14 (2021) 6774. https://doi.org/10.3390/ma14226774.
[29] A. Liu, J. Zou, Z. Wu, Y. Wang, Y. Tian, H. Xie, Enhancing the performance of TEG system coupled with PCMs by regulating the interfacial thermal conduction, Energy Reports 6 (2020) 1942–1949. https://doi.org/10.1016/j.egyr.2020.07.014.
[30] J.M. Park, D.Y. Hyeon, H.-S. Ma, S. Kim, S.-T. Kim, Y.N. Nguyen, I. Son, S. Yi, K.T. Kim, K.-I. Park, Enhanced output power of thermoelectric modules with reduced contact resistance by adopting the optimized Ni diffusion barrier layer, Journal of Alloys and Compounds 884 (2021) 161119. https://doi.org/10.1016/j.jallcom.2021.161119.
[31] P.H. Ngan, N. Van Nong, L.T. Hung, B. Balke, L. Han, E.M.J. Hedegaard, S. Linderoth, N. Pryds, On the Challenges of Reducing Contact Resistances in Thermoelectric Generators Based on Half-Heusler Alloys, J. Electron. Mater. 45 (2016) 594–601. https://doi.org/10.1007/s11664-015-4156-z.
[32] T.C. Holgate, L. Han, N. Wu, E.D. Bøjesen, M. Christensen, B.B. Iversen, N.V. Nong, N. Pryds, Characterization of the interface between an Fe–Cr alloy and the p-type thermoelectric oxide Ca3Co4O9, Journal of Alloys and Compounds 582 (2014) 827–833. https://doi.org/10.1016/j.jallcom.2013.08.096.
[33] N. Van Toan, T. Thi Kim Tuoi, N. Huu Trung, K. Fadzli Samat, N. Van Hieu, T. Ono, Micro-Thermoelectric Generators: Material Synthesis, Device Fabrication, and Application Demonstration, in: P. Vizureanu (Ed.), Latest Research on Energy Recovery, IntechOpen, 2023. https://doi.org/10.5772/intechopen.102649.
[34] Y. Shi, Y. Wang, D. Mei, B. Feng, Z. Chen, Design and Fabrication of Wearable Thermoelectric Generator Device for Heat Harvesting, IEEE Robot. Autom. Lett. 3 (2018) 373–378. https://doi.org/10.1109/LRA.2017.2734241.
[35] J. Cao, X.Y. Tan, N. Jia, J. Zheng, S.W. Chien, H.K. Ng, C.K.I. Tan, H. Liu, Q. Zhu, S. Wang, G. Zhang, K. Chen, Z. Li, L. Zhang, J. Xu, L. Hu, Q. Yan, J. Wu, A. Suwardi, Designing good compatibility factor in segmented Bi0.5Sb1.5Te3 – GeTe thermoelectrics for high power conversion efficiency, Nano Energy 96 (2022) 107147. https://doi.org/10.1016/j.nanoen.2022.107147.
[36] T. Hendricks, T. Caillat, T. Mori, Keynote Review of Latest Advances in Thermoelectric Generation Materials, Devices, and Technologies 2022, Energies 15 (2022) 7307. https://doi.org/10.3390/en15197307.
[37] G.J. Snyder, T.S. Ursell, Thermoelectric Efficiency and Compatibility, Phys. Rev. Lett. 91 (2003) 148301. https://doi.org/10.1103/PhysRevLett.91.148301.
[38] G.J. Snyder, Application of the compatibility factor to the design of segmented and cascaded thermoelectric generators, Applied Physics Letters 84 (2004) 2436–2438. https://doi.org/10.1063/1.1689396.
[39] P.H. Ngan, D.V. Christensen, G.J. Snyder, L.T. Hung, S. Linderoth, N.V. Nong, N. Pryds, Towards high efficiency segmented thermoelectric unicouples, Physica Status Solidi (a) 211 (2014) 9–17. https://doi.org/10.1002/pssa.201330155.
[40] S.R. Annapragada, T. Salamon, P. Kolodner, M. Hodes, S.V. Garimella, Determination of Electrical Contact Resistivity in Thermoelectric Modules (TEMs) From Module-Level Measurements, IEEE Trans. Compon., Packag. Manufact. Technol. 2 (2012) 668–676. https://doi.org/10.1109/TCPMT.2012.2183595.
[41] R. Liu, Y. Xing, J. Liao, X. Xia, C. Wang, C. Zhu, F. Xu, Z.-G. Chen, L. Chen, J. Huang, S. Bai, Thermal-inert and ohmic-contact interface for high performance half-Heusler based thermoelectric generator, Nat Commun 13 (2022) 7738. https://doi.org/10.1038/s41467-022-35290-6.

[42] S. Fujimoto, K. Nagase, H. Ohshima, M. Murata, A. Yamamoto, C.H. Lee, Thermoelectric Module of SiGe Bulk Alloys Forming p-n Junction at the Hot Side, Advanced Engineering Materials 24 (2022) 2101520. https://doi.org/10.1002/adem.202101520.
[43] J. Zhao, Z. Kuang, R. Long, Z. Liu, W. Liu, Impacts of thermal and electric contact resistance on the material design in segmented thermoelectric generators, Energy Storage and Saving 3 (2024) 5–15. https://doi.org/10.1016/j.enss.2023.12.001.
[44] Y. Li, Y. Shi, X. Wang, D. Luo, Y. Yan, Thermal and electrical contact resistances of thermoelectric generator: Experimental study and artificial neural network modelling, Applied Thermal Engineering 225 (2023) 120154. https://doi.org/10.1016/j.applthermaleng.2023.120154.
[45] L.T. Hung, N. Van Nong, S. Linderoth, N. Pryds, Segmentation of low-cost high efficiency oxide-based thermoelectric materials, Physica Status Solidi (a) 212 (2015) 767–774. https://doi.org/10.1002/pssa.201431626.
[46] R.A. Kishore, M. Sanghadasa, S. Priya, Optimization of segmented thermoelectric generator using Taguchi and ANOVA techniques, Sci Rep 7 (2017) 16746. https://doi.org/10.1038/s41598-017-16372-8.
[47] Z. Ouyang, D. Li, Design of segmented high-performance thermoelectric generators with cost in consideration, Applied Energy 221 (2018) 112–121. https://doi.org/10.1016/j.apenergy.2018.03.106.
[48] Z. Jin, Effective Interfacial Thermal and Electrical Resistances of a Microcracked Interface with Applications to Thermoelectrics, Physica Status Solidi (b) 258 (2021) 2000443. https://doi.org/10.1002/pssb.202000443.
[49] Z. Ouyang, D. Li, Modelling of segmented high-performance thermoelectric generators with effects of thermal radiation, electrical and thermal contact resistances, Sci Rep 6 (2016) 24123. https://doi.org/10.1038/srep24123.
[50] M.S. Dresselhaus, G. Chen, M.Y. Tang, R.G. Yang, H. Lee, D.Z. Wang, Z.F. Ren, J.-P. Fleurial, P. Gogna, New Directions for Low-Dimensional Thermoelectric Materials, Advanced Materials 19 (2007) 1043–1053. https://doi.org/10.1002/adma.200600527.
[51] N. Nakpathomkun, H.Q. Xu, H. Linke, Thermoelectric efficiency at maximum power in low-dimensional systems, Phys. Rev. B 82 (2010) 235428. https://doi.org/10.1103/PhysRevB.82.235428.
[52] Z.-H. Jin, Energy efficiency of thermoelectric materials: A three-dimensional study, Journal of Applied Physics 126 (2019) 085108. https://doi.org/10.1063/1.5111559.
[53] D.M. Rowe, ed., Thermoelectrics handbook: macro to nano, CRC/Taylor & Francis, Boca Raton, 2006.
[54] J. Zhang, D. Wu, D. He, D. Feng, M. Yin, X. Qin, J. He, Extraordinary Thermoelectric Performance Realized in n-Type PbTe through Multiphase Nanostructure Engineering, Advanced Materials 29 (2017) 1703148. https://doi.org/10.1002/adma.201703148.
[55] Y. He, T. Day, T. Zhang, H. Liu, X. Shi, L. Chen, G.J. Snyder, High Thermoelectric Performance in Non-Toxic Earth-Abundant Copper Sulfide, Advanced Materials 26 (2014) 3974–3978. https://doi.org/10.1002/adma.201400515.
[56] S. Roychowdhury, T. Ghosh, R. Arora, M. Samanta, L. Xie, N.K. Singh, A. Soni, J. He, U.V. Waghmare, K. Biswas, Enhanced atomic ordering leads to high thermoelectric performance in AgSbTe2, Science 371 (2021) 722–727. https://doi.org/10.1126/science.abb3517.
[57] G. Tan, F. Shi, S. Hao, L.-D. Zhao, H. Chi, X. Zhang, C. Uher, C. Wolverton, V.P. Dravid, M.G. Kanatzidis, Non-equilibrium processing leads to record high thermoelectric figure of merit in PbTe–SrTe, Nat Commun 7 (2016) 12167. https://doi.org/10.1038/ncomms12167.
[58] R. Liu, J. Yang, X. Chen, X. Shi, L. Chen, C. Uher, p-Type skutterudites RxMyFe3CoSb12 (R, M = Ba, Ce, Nd, and Yb): Effectiveness of double-filling for the lattice thermal conductivity reduction, Intermetallics 19 (2011) 1747–1751. https://doi.org/10.1016/j.intermet.2011.06.010.

[59] A. Zevalkink, J. Swallow, G.J. Snyder, Thermoelectric properties of Zn-doped Ca5In2Sb6, Dalton Trans. 42 (2013) 9713–9719. https://doi.org/10.1039/C3DT50428J.
[60] S. Ahmad, R. Basu, P. Sarkar, A. Singh, A. Bohra, S. Bhattacharya, R. Bhatt, K.N. Meshram, S. Samanta, P. Bhatt, M. Navaneethan, Y. Hayakawa, A.K. Debnath, S.K. Gupta, D.K. Aswal, K.P. Muthe, S.C. Gadkari, Enhanced thermoelectric figure-of-merit of p-type SiGe through TiO2 nanoinclusions and modulation doping of boron, Materialia 4 (2018) 147–156. https://doi.org/10.1016/j.mtla.2018.09.029.
[61] X. Shi, J. Yang, J.R. Salvador, M. Chi, J.Y. Cho, H. Wang, S. Bai, J. Yang, W. Zhang, L. Chen, Multiple-Filled Skutterudites: High Thermoelectric Figure of Merit through Separately Optimizing Electrical and Thermal Transports, J. Am. Chem. Soc. 133 (2011) 7837–7846. https://doi.org/10.1021/ja111199y.
[62] B. Jiang, X. Liu, Q. Wang, J. Cui, B. Jia, Y. Zhu, J. Feng, Y. Qiu, M. Gu, Z. Ge, J. He, Realizing high-efficiency power generation in low-cost PbS-based thermoelectric materials, Energy Environ. Sci. 13 (2020) 579–591. https://doi.org/10.1039/C9EE03410B.
[63] G.K. Goyal, S. Mukherjee, R.C. Mallik, S. Vitta, I. Samajdar, T. Dasgupta, High Thermoelectric Performance in Mg2(Si0.3Sn0.7) by Enhanced Phonon Scattering, ACS Appl. Energy Mater. 2 (2019) 2129–2137. https://doi.org/10.1021/acsaem.8b02148.
[64] B. Jabar, F. Li, Z. Zheng, A. Mansoor, Y. Zhu, C. Liang, D. Ao, Y. Chen, G. Liang, P. Fan, W. Liu, Homo-composition and hetero-structure nanocomposite Pnma Bi2SeS2 - Pnnm Bi2SeS2 with high thermoelectric performance, Nat Commun 12 (2021) 7192. https://doi.org/10.1038/s41467-021-27564-2.
[65] B. Jiang, X. Liu, Q. Wang, J. Cui, B. Jia, Y. Zhu, J. Feng, Y. Qiu, M. Gu, Z. Ge, J. He, Realizing high-efficiency power generation in low-cost PbS-based thermoelectric materials, Energy Environ. Sci. 13 (2020) 579–591. https://doi.org/10.1039/C9EE03410B.
[66] P.S. Thorup, C.M. Zeuthen, K.A. Borup, B.B. Iversen, Improving the Operational Stability of Thermoelectric Zn4Sb3 by Segmentation, Chem. Mater. 34 (2022) 5206–5214. https://doi.org/10.1021/acs.chemmater.2c00852.
[67] P. Gorskyi, Typical mechanisms of degradation of thermoelectric materials and ways to reduce their impact on the reliability of thermoelectric modules, Physics and Chemistry of Solid State 23 (2022) 505–516. https://doi.org/10.15330/pcss.23.3.505-516.
[68] M. Shtern, A. Sherchenkov, Y. Shtern, N. Borgardt, M. Rogachev, A. Yakubov, A. Babich, D. Pepelyaev, I. Voloshchuk, Y. Zaytseva, S. Pereverzeva, A. Gerasimenko, D. Potapov, D. Murashko, Mechanical properties and thermal stability of nanostructured thermoelectric materials on the basis of PbTe and GeTe, Journal of Alloys and Compounds 946 (2023) 169364. https://doi.org/10.1016/j.jallcom.2023.169364.
[69] X. Chen, H. Wu, J. Cui, Y. Xiao, Y. Zhang, J. He, Y. Chen, J. Cao, W. Cai, S.J. Pennycook, Z. Liu, L.-D. Zhao, J. Sui, Extraordinary thermoelectric performance in n-type manganese doped Mg3Sb2 Zintl: High band degeneracy, tuned carrier scattering mechanism and hierarchical microstructure, Nano Energy 52 (2018) 246–255. https://doi.org/10.1016/j.nanoen.2018.07.059.

Acknowledgments

D. V. C., N. P., V. E. and C.N.L. acknowledge the Danish Council for Independent Research Technology and Production Sciences for the DFF- Research Project 3 PILOT (Grant No 00069B). D.V.C. acknowledges the support of Novo Nordisk Foundation NERD Programme: New Exploratory Research and Discovery, Superior Grant NNF21OC0068015.

Highlights

- Thermoelectric (TE) material progress requires updated assessments of efficiency.
- Single and segmented TEs were evaluated considering their compatibility factors.
- Individual TEs can compete with segmented legs reaching record efficiencies of 17.9%.
- Segmentation can be an efficient approach if large thermal gradients are provided.
- The effects on efficiency are discussed if tolerable contact resistances are controlled.

.

Declaration of interests

☒ The authors declare that they have no known competing financial interests or personal relationships that could have appeared to influence the work reported in this paper.

☐ The authors declare the following financial interests/personal relationships which may be considered as potential competing interests: